

Reduced order modeling and large-scale validation for non-catalytic partial oxidation of natural gas

Yury Voloshchuk^a, Andreas Richter^{b,*}

^a CIC Virtuhcon, TU Bergakademie Freiberg, Fuchsmühlenweg 9 D, 09599 Freiberg, Germany

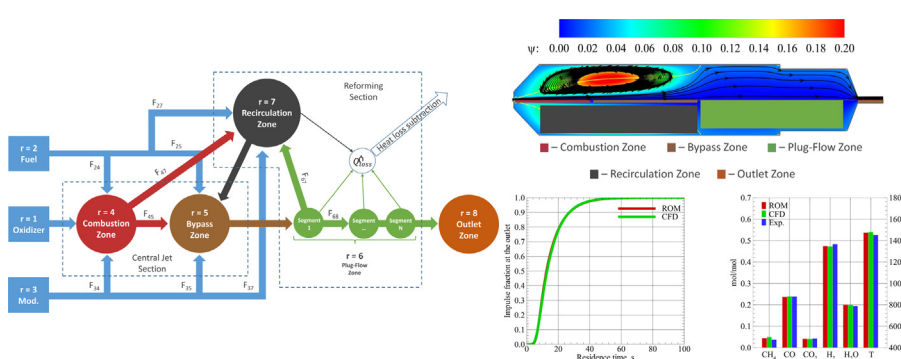
^b Institute of Energy Process Engineering and Chemical Engineering, Professorship for Modeling of Thermochemical Conversion Processes, TU Bergakademie Freiberg, Fuchsmühlenweg 9 D, 09599 Freiberg, Germany



HIGHLIGHTS

- Reduced order modeling of non-catalytic partial oxidation of natural gas.
- Low computational effort through a physics-based and compact model.
- Validation against semi-industrial test plant experiments and CFD.
- Demonstrated exibility and reliability of the model for a broad spectrum of operating parameters.
- Analysis of conversion processes in different reactor zones.

GRAPHICAL ABSTRACT



ARTICLE INFO

Article history:

Received 9 July 2021

Received in revised form 4 February 2022

Accepted 15 March 2022

Available online 2 April 2022

Keywords:

Non-catalytic partial oxidation

Reduced order model

Reactor network model

Industrial reformer

CFD

ABSTRACT

A reduced order model (ROM) for the non-catalytic partial oxidation (POX) of natural gas was developed and validated against large-scale numerical and experimental results. The ROM utilizes a network of perfectly stirred reactors, each describing a distinctive reactor zone and corresponding conversion processes. The zone definition is based on the CFD calculation of reactive flow, resulting in a compact, physics-based model that is valid for a broad range of POX reactors. The ROM is capable of predicting global reactor characteristics and flow field pattern within a short period of time, enabling the optimization of reactor geometry and the boundary and operating conditions. Additionally, the ROM can be used to evaluate detailed chemical reactions mechanisms. The ROM is validated against semi-industrial process data, and used to analyze the influence of each reactor zone on the overall species conversion. A new correlation between the fuel slip from the burner to the downstream reactor zones, the steam injection, and the λ value is built.

© 2022 Elsevier Ltd. All rights reserved.

1. Introduction

Partial oxidation (POX) of natural gas is a prevalent technology in the production of synthesis gas with a high hydrogen content. POX technology comprises non-catalytic and catalytic implemen-

tation. In both variants, the natural gas and oxygen are injected via a burner into the reactor where the partial oxidation, steam reforming and water-gas-shift reactions occur (Higman and van der Burgt, 2003). The non-catalytic implementation allows the natural gas to be reformed in a wide range of operating conditions. Catalytic POX, commonly known as autothermal reforming (ATR), provides high-quality synthesis gas and operates at lower temperatures, but is critical to the natural gas quality. In ATR, reforming

* Corresponding author.

E-mail address: a.richter@iec.tu-freiberg.de (A. Richter).

Nomenclature

A	Numeration lambda function	h	Specific enthalpy
A	Wall surface area	h_t	Wall heat transfer coefficient
B	Denomination lambda function	m	PSR's content mass
C_{st}	Stoichiometric criterion	n	Stoichiometric coefficient
F	Mass flow rate fraction	p	Pressure
K_{DO}	Correction factor for diffusion flame with concentrically supplied oxygen	u_k	Specific internal energy
K_{ID}	Correction factor for isolated diffusion flame	$u_{F,M}$	Velocity of fuel or moderator
L	Length	u_O	Velocity of oxidizer
N	Total number of solutions	z	Mixture fraction
T	Temperature	O	Inlet
V	Volume	N_{inlet}	Total number of inlets
$V_{segment}$	Single segment volume	N_{outlet}	Total number of outlets
W	Species molecular weight	atm	Surrounding fluid, reactor atmosphere
Y	Species mass fraction	st	Stoichiometry
Y_{O_2}	Mass fraction of oxygen	i	Inlet's index number
Y_C	Mass fraction of combustible species	j	Outlet's index number
χ	Conversion fraction	k	Species index number
Q_{loss}	Heat loss	r	PSR's index number
\dot{V}	Volumetric flow rate	r'	Downstream PSR's index number
$\dot{\omega}$	Species molar production rate	bpz	Bypass zone
\dot{m}	Mass flow rate	cz	Combustion zone
$\dot{m}_{O_2}^0$	Inlet mass flow rate of oxygen	oz	Outlet zone
\dot{m}_C^0	Inlet mass flow rate of combustible species	pfz	Plug-flow zone
λ	Lambda value	rz	Recirculation zone
ϕ	Equivalence ratio	F	Fuel
ρ	Density	M	Moderator
τ	Residence time	O	Oxidizer
c_v	Heat capacity at constant volume		
d	Diameter		

reactions are intensified by a catalytic bed (Aasberg-Petersen et al., 2001). The main advantage of non-catalytic POX compared to ATR is its flexibility. It can be operated in a wide range of operating conditions and for several feedstocks, and allows single-stage natural gas reforming without a catalyst (Ullman's Encyclopedia of Industrial Chemistry, 2003; Aasberg-Petersen et al., 2001). Non-catalytic POX is widely used in industrial processes (Peña et al., 1996; van Helvoort and Senden, 2014; van der Burgt et al., 1988).

POX technology has been intensively studied experimentally and numerically due to increasing interest in the processing of natural gas. Most experimental studies, however, are limited to lab-scale equipment and aim to evaluate specific processes occurring in the reactor. Bustamante et al. (2004) investigated the parameters of the reverse water-gas-shift reaction in a lab-scale quartz reactor. Han et al. (2010) studied methane combustion mechanism under POX conditions. Li et al. (2013), Li et al. (2018) discussed the influence of process variables on methane conversion. Zhai et al. (2010) performed a numerical and experimental study of a micro-reactor for methane steam reforming.

Only few experimental studies conducted under industrially relevant conditions, meaning operating pressures above 50 bar and large reactor volumes with a wide residence time distribution, are available. However, such studies are mostly limited to the global reactor characteristics. Xu et al. (2014) presented large-scale POX experiments. The outlet gas composition and temperature were used to validate numerical models. Richter et al. (2015) conducted large-scale experiments that included comprehensive information about the burner, reactor geometry, and operating conditions. Measurements were carried out of the temperature along the reactor wall and the species concentration at the reactor

outlet. Additionally, in-situ optical measurements of the flame region were carried out. Förster et al. (2017) conducted experimental and numerical studies of the same large-scale POX reactor with different nozzles.

With rapidly changing environmental and economical regulations, the usual path of technological development from small-scale to demo-scale, and finally on to industrial-scale is no longer feasible. Nowadays, numerical investigation techniques such as computational fluid dynamics (CFD), equilibrium, kinetic, and reduced order models (ROM), are used to predict and analyze the new process.

Equilibrium models can provide a rapid solution and are commonly used in chemical engineering to estimate the system's thermo-chemical state. Equilibrium models utilize the Gibbs free energy minimization method and do not require considerable computational power. They do not take into account chemical kinetics and are therefore not capable of providing detailed information about inner reactor processes like CFD models. However, equilibrium models are useful in simulating complex process chains for fundamental analysis (Velasco et al., 2014; Aminand and Yaw, 2007; Siang et al., 2020).

Kinetic models include 0D and 1D modeling approaches and are capable of accounting for chemical kinetics. Mostly, kinetic studies are dedicated to developing modeling approaches for the process evaluation and sub-models for CFD calculations, e.g., detailed chemical mechanisms, heat transfer, and particle treatment models (Yu et al., 2006; Olivieri and Veglio, 2008; Zamaniyan et al., 2008; Nezhad et al., 2009; Brüggemann et al., 2010).

The CFD models can provide a detailed solution resolving the species transport, reactive flow, reaction kinetics, heat transfer,

and other phenomena (Rehm et al., 2009; Xu et al., 2014; Vascellari et al., 2015; Voloshchuk et al., 2017). While CFD models provide extensive information about inner reactor processes, kinetic and equilibrium models provide fundamental and simplified information on the system. However, none of the approaches is suitable for the reactor optimization – CFD due to the computational effort, and equilibrium and kinetic models due to the oversimplified processes.

A numerical model that is suitable for reactor optimization must be able to consider complex chemical kinetics, reproducing reactor flow patterns such as recirculation, plug-flow, jet-flow, and heat and mass transfer, while having a low computational cost. The latter is important since optimization often involves multiple configurations of boundary conditions and reactor geometries that require numerous simulation runs.

Reduced Order Models (ROMs) combine 0D and 1D approaches to create a comprehensive modeling network. The ROM can provide necessary information on the process at a low computational costs; it can be coupled with optimization algorithms and perform thousands of calculations within a short period of time. However, there are only a limited number of studies describing ROMs for reactive systems. Most of the proposed models are built to test sub-models for CFD calculations or novel chemical mechanisms and are unable to reproduce the basic physics of the reaction chamber.

Pedersen et al. (1997) presented the concept of an ideal chemical reactors network based on CFD calculations of a 160 kW test furnace. Later, this model was validated against experiments from the same facility (Pedersen et al., 1998). In the work of Monaghan and Ghoniem (2012), a reduced order model for an entrained-flow gasifier was developed. In this model, the reactor was divided into six zones, each represented by perfectly stirred or plug flow reactors. Later, this model was validated in the second part of the study (Monaghan and Ghoniem, 2012). Toni et al. (2013) developed a chemical reactor network model for the BERL furnace (Fornaciari et al., 1994; Silva, 2003). The reactor was divided into five parts: the flame front, post flame, outlet plug flow, recirculation and inner recirculation zones. Each of the models discussed was developed for specific reactors and is hard to adapt for other reactor types.

In the present work, a novel reduced order model is built based on previous CFD and experimental studies. Contrary to several reduced order models discussed in literature, the inlet streams dissipation upon entering the reaction chamber is taken into account, and the fuel and the moderator slip are estimated prior to the combustion zone calculations without the help of CFD. Also, a nozzle dependent combustion zone calculation is implemented. The ROM defines the zones internally based on the boundary conditions, and does not require a zone volume definition by hand. Such an approach allows for a reactor calculation without user input or additional tuning work. The model is optimized using a two-stage optimization procedure and is extensively validated against numerical results and experiments. The validation shows that the model can be used for different reactor and nozzle geometries without additional optimization loops for stream functions, which makes the ROM a unique stand-alone tool for calculations of the natural gas partial oxidation systems.

The ROM is described in Section 2, listing the general assumptions made and discussing the coupling of the model with an optimization algorithm. Additionally, a sensitivity analysis is described, and the influence of each zone on the reactor characteristics is shown. In Section 3, the ROM is validated against experiments and CFD, and the advantages and disadvantages of the developed ROM are discussed. Finally, in Section 4, a summary of the current research is given and conclusions are drawn regarding the inner POX processes based on the ROM results that are obtained.

2. Reduced order model

2.1. Experimental reference data

The numerical models are in line with experimental data that are obtained from a semi-industrial high-pressure partial oxidation reactor at TU Bergakademie Freiberg. The advantages of this test facility are the comprehensive measuring techniques and possibility to adjust the reactor volume and the burner geometry. The experimental results are described in detail in (Richter et al., 2015; Voloshchuk et al., 2017). Cases 1–4 are based on the Virtuhcon Benchmark (Richter et al., 2015), which has a reactor volume of 450 l. Cases 5–8 were conducted at the same facility. However, the reactor and nozzle geometries were changed to validate the model. The results for Case 5 were published in (Förster et al., 2017). Herewith, the reactor volume was significantly reduced to 41 l. Cases 6–8 reflect a similar configuration, but with a modified burner geometry, resulting in oxidizer velocities that are increased by a factor of 3 and 5 compared to the previous setups.

2.2. Definition of reactor zones

The ROM was developed based on the experimental and numerical study of the Virtuhcon Benchmark (Richter et al., 2015; Voloshchuk et al., 2017). In this large-scale high-pressure, high-temperature process, the reactants are injected using a multichannel burner as shown in Fig. 1. Three streams – natural gas as the fuel, steam as the moderator, and oxygen premixed with steam as the oxidizer – mix with each other milliseconds after entering the reactor. This starts the oxidation reactions and thus the ignition

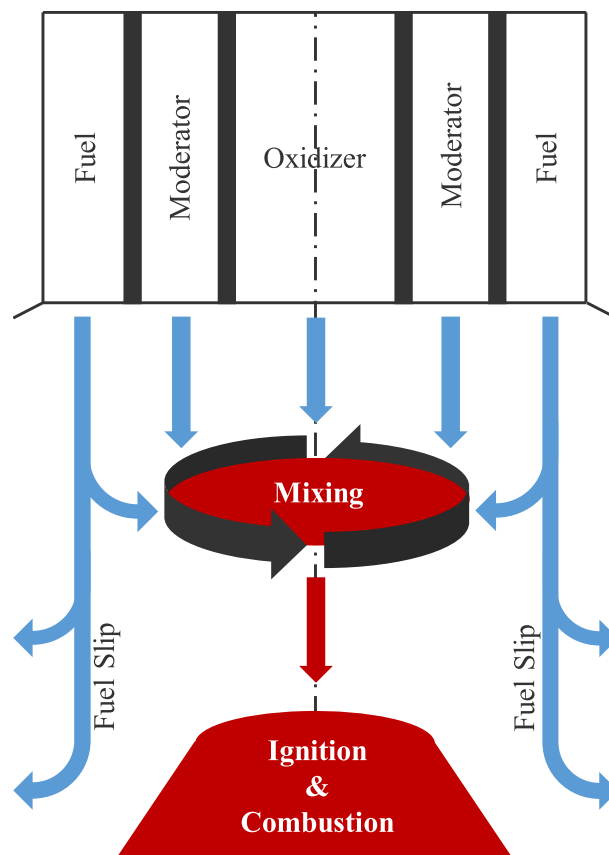


Fig. 1. Diagram of a reactants mixing mechanism for a typical nozzle configuration with concentrically supplied oxygen used in the POX reactor (Voloshchuk et al., 2017).

of the mixture. The oxidation reactions continue until one of the initial reactants is fully consumed (Richter et al., 2015; Voloshchuk et al., 2017).

In order to identify the zones of the reactor, the stream function was extracted from the CFD results (Voloshchuk et al., 2017). Additionally, streamlines and zero axial velocity boundary were built depicting the fluid trajectories (see Fig. 2).

As depicted in the flow field shown in Fig. 2, there is a recirculation of gas in the reactor. Streamlines indicate that the recirculation zone is characterized by the complete circular motion of the fluid. A zero axial velocity boundary splits this zone into two regions. This boundary is illustrated in Fig. 2 and marked as a zero axial velocity border. The region located between the boundary and the wall is the region of negative axial velocities, which means that the fluid flows toward the burner at that point. The other region is the region of positive axial velocities. The point where zero axial velocity curve meets the reactor wall defines the length of the recirculation zone. From that point further downstream, the fluid motion is like that in a plug-flow reactor. In addition, the central jet is stable almost to the end of the recirculation zone, where it diverges into the plug-flow. The central jet combines the combustion zone and the so-called bypass zone. Based on the analysis of the streamlines, zero axial velocity boundary and stream function, the reactor was divided into five zones as shown in Fig. 2. Each zone was considered to be cylindrical to simplify the calculations.

From the empirical study (Cerbe and Lendt, 2016), the volume of the combustion zone reads as:

$$V_{cz} = L_{cz} \frac{\pi d_{cz}^2}{4}, \quad (1)$$

where L_{cz} is the length and d_{cz} is the diameter of the combustion zone. In the work of Cerbe and Lendt (2016), an empirical Eq. 2 was proposed for the calculation of the flame length. Taking into account stoichiometric combustion conditions, Eq. 2 is used to calculate the combustion zone length and define the combustion frontier. L_{cz} is the length of the combustion zone and is defined as:

$$L_{cz} = \frac{z_0}{z_{st}} \frac{c_M}{2c_H^2} d_0 \sqrt{\frac{\rho_0}{\rho_{atm}}} K_{id} K_{Do}, \quad (2)$$

where z_0 is the mixture fraction at the inlet, z_{st} is the stoichiometric mixture fraction, d_0 is the hydraulic diameter of the nozzle, $c_M = 0.075$ and $c_H = 0.087$ (Cerbe and Lendt, 2016) are the transfer coefficients for momentum and heat, respectively, for natural gas, ρ_0 and ρ_{atm} are the densities of the fluid at the nozzle and surround-

ing atmosphere, respectively, K_{id} is the non-dimensional correction factor for an isolated diffusion flame, and K_{Do} is the non-dimensional correction factor for a diffusion flame with concentrically supplied oxidizer. K_{id} is defined as:

$$K_{id} = 0.065 \frac{\dot{m}_O + \dot{m}_M}{\dot{m}_O + \dot{m}_M + \dot{m}_F} \frac{d}{d_0} + 0.95, \quad (3)$$

where \dot{m}_O , \dot{m}_M , and \dot{m}_F are the mass flow rates of the oxidizer, moderator, and fuel, respectively, and d is the diameter of the reactor. The K_{Do} reads as:

$$K_{Do} = 1 - \left(\frac{u_{F,M}}{u_O} \right)^{1.6}, \quad (4)$$

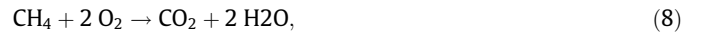
where $u_{F,M}$ is the velocity of the fuel and moderator, and u_O is the velocity of the oxidizer. The K_{Do} term is applied only if $u_O > u_{F,M}$. The stoichiometric mixture fraction z_{st} is calculated as:

$$z_{st} = \frac{1}{1 + \phi}, \quad (5)$$

where ϕ is the equivalence ratio, defined as:

$$\phi = n \frac{\dot{m}_c^0}{\dot{m}_{O_2}^0}, \quad (6)$$

where \dot{m}_c^0 is the mass flow rate of the combustible species at the inlet, $\dot{m}_{O_2}^0$ is the mass flow rate of the oxygen at the inlet, and n is the stoichiometric coefficient calculated from the following global reactions:



In the current study, the fuel mass flow rate at the inlet of the combustion zone is assumed to correspond to the stoichiometric mass flow rate of combustible species. Thus, only a fraction of the total fuel mass flow is injected into the combustion zone. The rest of the fuel flows to other zones.

Fig. 3 shows the temperature distribution in the vicinity of the burner (Voloshchuk et al., 2017). The diameter of the combustion zone, calculated from the stoichiometric combustion frontier and depicted by the black curve, does not exceed the nozzle diameter, marked by red lines. The change in the combustion zone diameter is not taken into account in the present study since the difference in diameters between the nozzle and the combustion zone is negligible. Therefore, $d_0 = d_{cz}$ in Eq. 1.

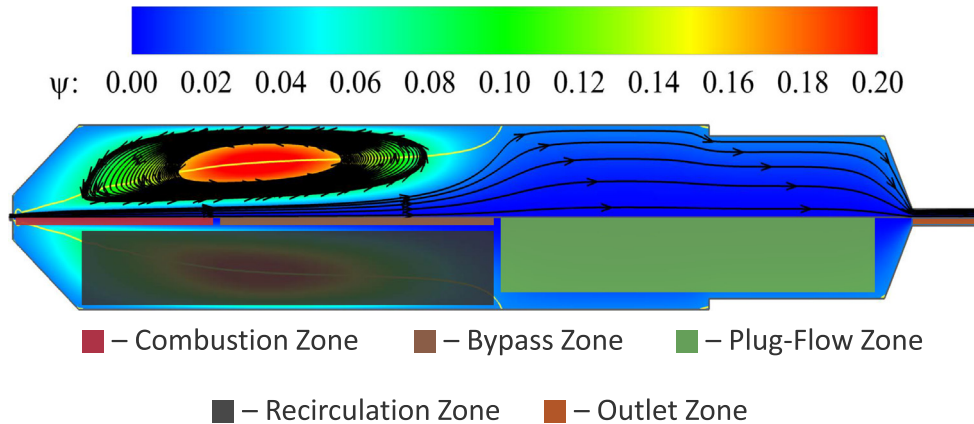


Fig. 2. Stream function of Virtuhcon Benchmark reactor obtained from 2D axis-symmetric CFD simulation (Voloshchuk et al., 2017). Top half shows stream function ψ and streamlines. Yellow curve indicates zero axial velocity border. Bottom half indicates different zones.

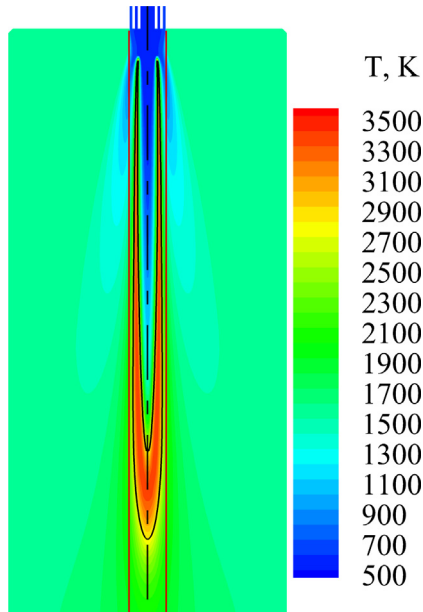


Fig. 3. Temperature distribution in the vicinity of the burner (Voloshchuk et al., 2017). The solid black curve marks the stoichiometric combustion frontier. The red lines indicate the external diameter of nozzle.

The volume of the bypass zone is calculated considering the diameter of the combustion zone:

$$V_{bpz} = L_{bpz} \frac{\pi d_{cz}^2}{4}, \quad (10)$$

where L_{bpz} is the length of the bypass zone, calculated as:

$$L_{bpz} = (1 - K_{pfz})(L - L_{oz}) - L_{cz}, \quad (11)$$

where L is the total length of the reaction chamber and L_{oz} is the length of the outlet zone, taken from reactor geometry. K_{pfz} is the plug-flow length coefficient, defined as a fraction of the reactor length occupied by the plug-flow zone:

$$K_{pfz} = \frac{L - L_{oz} - L_{rz}}{L - L_{oz}}, \quad (12)$$

where L_{rz} is the length of the recirculation zone, defined by the zero axial velocity boundary. It should be noted that $L_{rz} \approx \text{const.}$ and $K_{pfz} \approx 0.46$ for all Virtuhcon Benchmark cases. The volume of the plug-flow zone reads:

$$V_{pfz} = \pi K_{pfz} (L - L_{oz}) \frac{d^2}{4}. \quad (13)$$

The volume of the outlet zone is defined as:

$$V_{oz} = \pi L_{oz} \frac{d_{oz}^2}{4}, \quad (14)$$

where V_{oz} is the volume of the outlet zone and d_{oz} is the diameter of the outlet. The volume of the recirculation zone is subtracted from the total reactor volume:

$$V_{rz} = V - (V_{cz} + V_{bpz} + V_{pfz} + V_{oz}), \quad (15)$$

where V_{rz} is the volume of the recirculation zone and V is the total volume of the reaction chamber.

2.3. Model assumptions

One of the main assumptions behind the development of the ROM is that all exothermic reactions between the fuel and oxidizer

take place only in a certain region of the central jet named the *combustion zone*. The combustion zone, in turn, is defined by the *combustion frontier*. It is assumed that no exothermic reactions occur beyond the combustion frontier since all oxygen is consumed. At that frontier, temperatures over 3000 K can occur, defining the core of the flame (Voloshchuk et al., 2017). In the literature, the flame is usually characterized by temperature gradients or OH concentration (Yang et al., 2021; Somaratne et al., 2020; Guiberti et al., 2020). Herewith, the flame length estimation using temperature gradients or OH concentration is subjective since it depends on freely manipulative criteria, e.g., the highest temperature peak or lowest OH concentration. On the other hand, the stoichiometric definition of the combustion zone is certain, as it is defined by the chemistry. Richter et al. (2015) observed the flame by means of an optical probe system. However, due to a lack of experimental information and as technology cannot be used in such a harsh environment, the definition of the flame front is a matter of controversy. Another assumption of the ROM is that there is no backward interaction between the surrounding atmosphere and the combustion zone. Thus, the combustion frontier is defined only by stoichiometry and is not influenced by the recirculation of reforming products.

Fuel is injected through an outer ring using a multichannel burner (see Fig. 1). In this case, some of the fuel escapes mixing zone and goes directly to the recirculation zone. This phenomenon is called the *fuel slip*. In the present study, the fuel slip phenomenon is taken into account by injecting fuel separately into different reactor zones.

The use of ROM allows calculations to be made with detailed chemical mechanisms due to the rapid speed of each single simulation. In this work, the GRI 3.0 reaction mechanism is applied (Smith et al., 1999). This mechanism includes 325 elementary reactions and consists of 53 species.

2.4. Modeling approach

In this study, an object-oriented software toolkit named Cantera® for chemical kinetics, thermodynamics and transport processes is used to solve the governing equations (Goodwin et al., 2018). All the reactor zones are modeled as perfectly stirred reactors (PSR), as shown in Fig. 4. The mass conservation equation for a single PSR reads as:

$$\frac{dm_{(r)}}{dt} = \sum_{i=1}^{N_{\text{inlet}(r)}} \dot{m}_{i(r)} - \sum_{j=1}^{N_{\text{outlet}(r)}} \dot{m}_{j(r)}, \quad (16)$$

where $m_{(r)}$ is the PSR's content mass with the index number r , \dot{m} is the mass flow rate, N_{inlet} and N_{outlet} are the total number of inlets and outlets in the reactor, respectively, and i and j are the inlet and the outlet index numbers, respectively. The species conservation equation reads as:

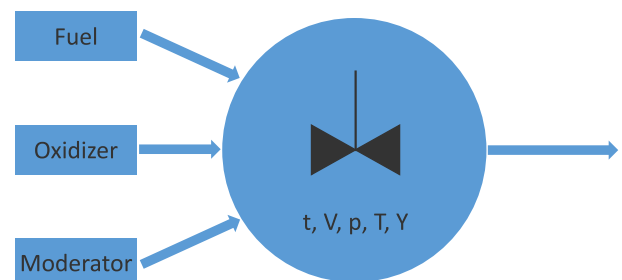


Fig. 4. Diagram of the perfectly stirred reactor.

$$\frac{d(m_{(r)} Y_{k(r)})}{dt} = \sum_{i=1}^{N_{\text{inlet}(r)}} \dot{m}_{i(r)} Y_{k(r),i} - \sum_{j=1}^{N_{\text{outlet}(r)}} \dot{m}_{j(r)} Y_{k(r)} + V_{(r)} \dot{\omega}_{k(r)} W_k \quad (17)$$

where Y_k is the mass fraction of the k^{th} species, $V_{(r)}$ is the volume of the PSR r , $\dot{\omega}_k$ is the molar production rate of the k^{th} species, and W_k is the molecular weight of the k^{th} species. The energy conservation equation is solved as:

$$m_{(r)} c_v \frac{dT_{(r)}}{dt} = -p \frac{dV_{(r)}}{dt} - \dot{Q}_{\text{loss}} + \sum_{i=1}^{N_{\text{inlet}(r)}} \dot{m}_{i(r)} \left(h_i - \sum_k u_k Y_{k(r),i} \right) - \frac{pV_{(r)}}{m_{(r)}} \sum_{j=1}^{N_{\text{outlet}(r)}} \dot{m}_{j(r)} - V_{(r)} \dot{\omega}_{k(r)} W_k u_k, \quad (18)$$

where T is the temperature of the PSR r , p is the pressure, \dot{Q}_{loss} is the heat losses, h is the specific enthalpy and c_v is the heat capacity at constant volume, and u_k is the specific internal energy of species k . Heat losses are calculated as:

$$\dot{Q}_{\text{loss}} = Ah_t(T - T_0) \quad (19)$$

where A is the wall surface area, h_t is the heat transfer coefficient, and T and T_0 are the gas and ambient temperatures, respectively.

2.5. Coupling of zones

Fig. 5 shows the coupling scheme used in the ROM. An index number r is assigned to each PSR. To couple all the reactor zones, mass stream functions must be defined, as depicted in Fig. 5. These functions represent the mass flow rates between related PSRs. The information regarding boundary conditions such as the reactant composition, temperature, and pressure, are stored in three reservoirs: $r = 1, r = 2$, and $r = 3$, indicated by blue rectangles (see Fig. 5).

The mass stream function reads as:

$$\dot{m}_{rr'} = F_{rr'} \sum_{j=1}^{N_{\text{outlet}(r)}} \dot{m}_{j(r)}, \quad (20)$$

where $\dot{m}_{rr'}$ and $F_{rr'}$ are the mass flow rate and the mass flow rate fraction from the current zone r to the downstream zone r' , respectively. The mass flow rate fraction $F_{rr'}$ is defined independently of the pressure, volume or any other characteristics, and represents the fraction of mass transported from one zone to another. In Fig. 5, each zone is marked with a specific color to help the reader navigate. These colors are also applied to the outlet mass stream functions of related PSRs. For instance, combustion zone ($r = 4$) has three inlet streams coming from oxidizer ($r = 1$), fuel ($r = 2$) and moderator ($r = 3$) reservoirs, indicated in blue, and has two outlets indicated in red color – the color of the combustion zone ($r = 4$).

The ROM is divided into two sections, as shown in Fig. 5. One is the central jet section, which comprises the combustion and bypass zones. Another is the reforming section, which includes the recirculation and plug-flow zones. The outlet zone can also be included in the reforming section, but since the reaction rates are negligible, it is examined as a stand-alone zone in this study. The sections are used in post-processing.

Preliminary studies showed that the plug-flow zone ($r = 6$) plays a defining role in resolving the basic flow pattern and significantly affects species conversion. Therefore, the plug-flow zone ($r = 6$) is simulated as a cascade of PSRs. This approach does not require additional assumptions and does not result in increased computational effort. The plug-flow zone is marked in green in Fig. 5. The number of segments results from a numerical study and is the optimum compromise between minimum computational effort and maximum accuracy. The volume of a single segment is defined by:

$$V_{\text{segment}} = \frac{V_{\text{pfz}}}{n}, \quad (21)$$

where n is the number of segments in the plug-flow cascade.

Fig. 6 depicts the methane and temperature distribution in the plug-flow zone.

The temperature difference between the first and the last segments of the plug-flow cascade is more than 200 K, while the methane content varies within 2%. Thus, the position of the mass stream function F_{67} is crucial for correctly modeling the recirculation zone. In this case, the first segment of the plug-flow cascade

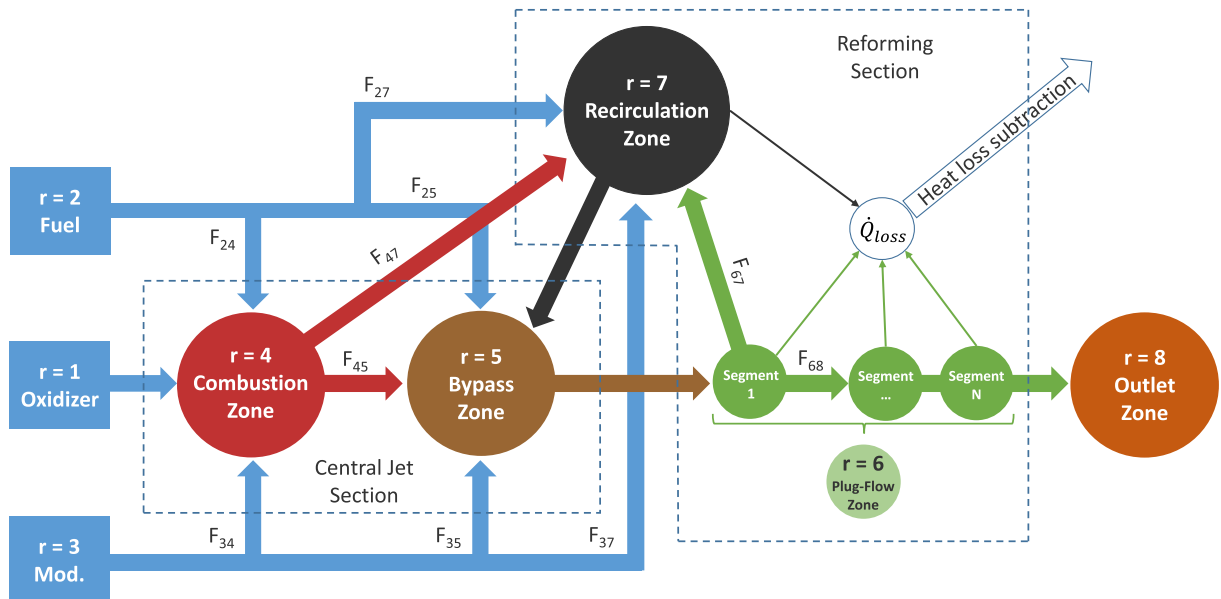


Fig. 5. Coupling scheme of the Reduced Order Model. The circles denote PSR and the rectangles denote non-reactive reservoirs. Arrows indicate the fraction of a mass flow transported between PSRs.

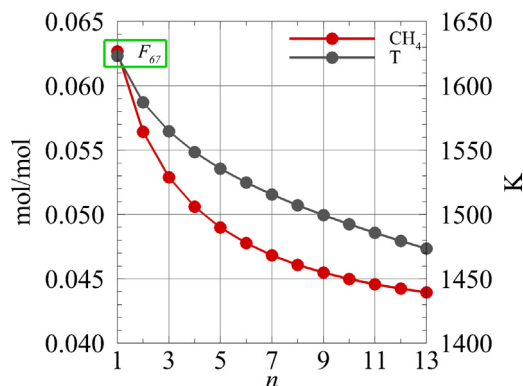


Fig. 6. Distribution of CH_4 and temperature in the plug-flow zone. The green rectangle indicates a stage at which gas properties are taken for the mass transfer function F_{67} .

plays an important role and acts like a transition zone from recirculating to a fully developed plug flow. The heat losses are applied to the recirculation zone ($r = 7$) and plug-flow zone ($r = 6$), since, apart from the negligibly small outlet zone ($r = 8$), only recirculation and plug-flow zones are surrounded by the wall. Table 1 shows the input characteristics used in the ROM, CFD and experiments for all the cases calculated in the present study. The set of experimental and CFD data comprises of eight test cases. The reactor geometry is constant for cases 1–4. Cases 5–8 are aimed on testing the ROM capability of predicting results for different reactor geometries and different oxidizer and fuel rates. Here the λ shows a ratio between actual oxygen-fuel ratio and stoichiometric oxygen-fuel ratio for a given mixture. For the cases 1–3, λ value is almost constant, while for cases 4–8 the value is significantly higher. This allows for comparison of the results for different mixtures.

λ is calculated as:

$$\lambda = \frac{m_{\text{O}_2}/m_{\text{fuel}}}{(m_{\text{O}_2}/m_{\text{fuel}})_{\text{st}}}, \quad (22)$$

where m_{O_2} is the mass of the oxygen, m_{fuel} is the mass of the fuel, st subscript denotes stoichiometric conditions.

2.6. Model optimization – combustion zone

In this section, only the combustion zone is taken into account. The combustion zone calculations are carried out for the nozzle concept with the concentrically supplied oxidizer (see Fig. 1). The nozzle geometry does not change for cases 1–4, but slightly differs for cases 5–8. However, these differences and corresponding hydraulic diameters and stream velocities are considered in non-dimensional correction factors K_{ID} and K_{DO} (see Eq. 3 and Eq. 4).

First, the length of the combustion zone is calculated by Eq. 2. The streams variations are done independently from the nozzle

characteristics. However, the influence of the nozzle on the combustion zone is considered in the combustion zone volume calculations. It is important to validate this approach against CFD results. Table 2 lists combustion zone lengths for different cases estimated from the combustion frontier. As shown, the ROM and CFD results are in good agreement. The biggest difference is observed for Case 4. However, the difference is negligible in comparison to the overall length of the reactor. This means that the approach proposed by Cerbe and Lendt (2016) is valid for all simulated cases and can predict the combustion zone length calculated by CFD.

The amount of fuel needed for stoichiometric combustion cannot be estimated easily due to the influence that the additional steam injected in the combustion zone has on the species conversion and temperature. As shown in Fig. 7, the stoichiometry is coupled with the amount of steam entering the combustion zone. Each mass stream fraction F_{rr} (see Fig. 5) can vary between 0 and 1, which results in a large number of variations. Despite the fact that a single ROM simulation takes only a few seconds, calculating all possible stream configurations can be extremely time-consuming. Therefore, an optimization procedure is necessary in order to define the F_{rr} values. Fig. 8 shows the optimization procedure that is included in the overall reactor model to define the combustion zone.

The combustion zone is simulated as an isochoric PSR ($r = 4$). The oxidizer stream is injected into the combustion zone. However, the fuel and moderator streams F_{24} and F_{34} vary to reach stoichiometric conditions. The streams variations are independent from the nozzle characteristics. However, the influence of the nozzle on the combustion zone is considered in the combustion zone volume calculations. Once stoichiometry is reached, the F_{24} and F_{34} values are extracted, and the optimization proceeds to the second stage.

To check for compliance with stoichiometric conditions, the stoichiometric criterion is implemented. The stoichiometric criterion shows how much of the combustible species and oxygen are consumed in the combustion zone:

$$C_{\text{st}} = \min \{C_{\text{sti}}\}_{i=1}^N; \quad C_{\text{sti}} = Y_{\text{Ci}}^{r=4} + Y_{\text{O}_2i}^{r=4}, \quad (23)$$

where C_{st} is the stoichiometric criterion, i is the index number of the solution in the array, N is the total number of solutions in the array, Y_{C} is the mass fraction of combustible species, Y_{O_2} is the mass fraction of O_2 , $r = 4$ is the combustion zone index number in the coupling scheme in Fig. 5.

2.7. Sensitivity study on the combustion zone

The fuel mass flow rate fraction F_{24} (see Fig. 5) is varied in the range from 45% to 65% for the first three cases, and from 55% to 75% for Case 4, since the outlet temperature and the amount of O_2 injected into the system are higher. The moderator mass flow rate fraction F_{34} is fixed to three values in order to reduce computational effort. $F_{34} = 0$ means that no moderator enters the com-

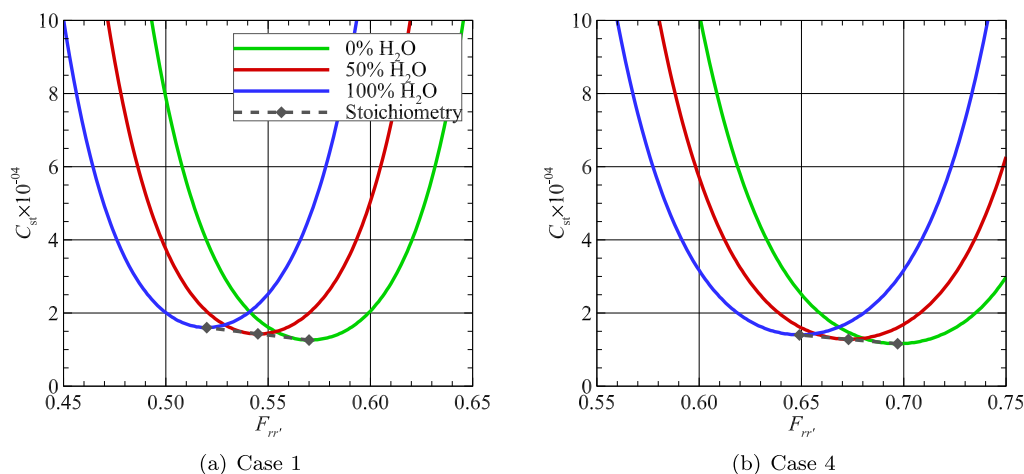
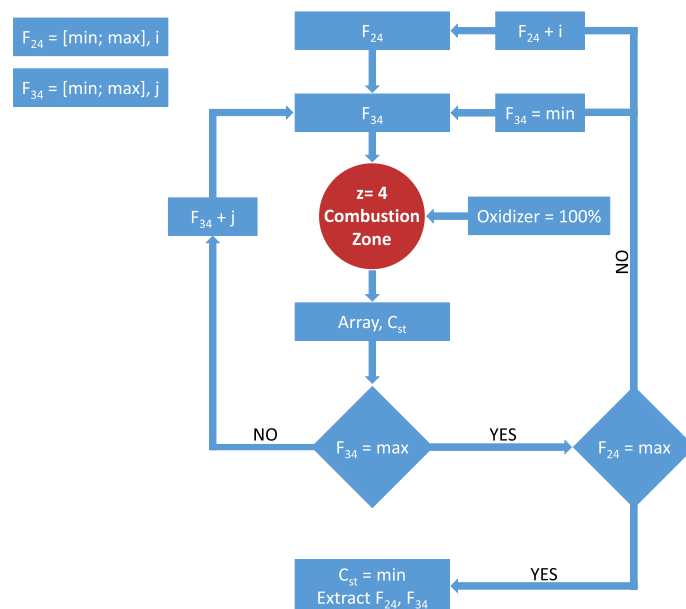
Table 1
Input characteristics for Cases 1–8.

	Case 1	Case 2	Case 3	Case 4	Case 5	Case 6	Case 7	Case 8
<i>Operating conditions</i>								
Pressure, bar(g)	50	60	70	50	60	40	40	40
λ	0.314	0.313	0.305	0.387	0.388	0.383	0.348	0.374
Temperature, K	1473	1473	1473	1673	1690	1696	1638	1685
Reactor volume, m ³	0.45	0.45	0.45	0.45	0.04	0.12	0.12	0.12
Residence time, s	15.96	16.12	16.22	14.80	1.22	2.55	2.63	1.81
<i>Thermal characteristics</i>								
Input energy flow rate, kW	3110	3726	4353	2726	3675	3045	3029	4572

Table 2

Combustion zone length for different cases.

	Case 1	Case 2	Case 3	Case 4
Cerbe and Lendt (2016), mm	220	224	220	266
CFD, mm	227	227	227	252
Δ , mm	7	3	7	14

**Fig. 7.** Sensitivity of stoichiometric criterion to fuel and moderator in the combustion zone. Blue, red, and green graphs show influence of fuel injection on stoichiometric criterion when 100%, 50%, and 0% of moderator is injected in the combustion zone, respectively. Gray line shows the position at which stoichiometric criterion is satisfied.**Fig. 8.** Diagram of the first stage of the ROM optimization.

bustion zone. $F_{34} = 0.5$ means that only 50% of the moderator enters the combustion zone. $F_{34} = 1$ means that all the moderator enters the combustion zone. The results of the sensitivity study are shown in Fig. 7. It is clearly observed that the stoichiometric criterion depends linearly on the moderator injection. Thus, the greater the amount of moderator involved in the combustion process, the higher the value of the stoichiometric criterion and, consequently, the fuel slip. This means that injecting the moderator into the combustion zone reduces the fuel conversion via oxidation.

Table 3 denotes fuel slip from the combustion zone depending on the amount of steam injected. The difference between first three

cases is the operating pressure. It increases from 50 to 60, and to 70 bar, respectively, while λ remains nearly constant. The lowest fuel slip is observed when no H_2O is involved in the combustion process. This conclusion is valid for all simulated cases.

The effect which the amount of steam has on the fuel slip can be explained by analyzing H_2O - and OH -related reactions paths. This analysis was carried out in ChemkinPro (ANSYS, 2016), a software package for the analysis of gas-phase chemical and plasma kinetics. The combustion zone was simulated as a PSR with boundary conditions taken from the first stage of optimization, and the GRI 3.0 reaction mechanism (Smith et al., 1999) was used. The amount

Table 3

Fuel slip defined by stoichiometric criterion.

Injected H ₂ O, F_{34}	Case 1	Case 2	Case 3	Case 4
Pressure, bar	50	60	70	50
0%	0.430	0.437	0.451	0.303
50%	0.455	0.461	0.476	0.327
100%	0.480	0.486	0.501	0.351

of fuel and oxidizer injected into the PSR were constant, but the amount of steam was varied to assess its effects on the production rates of minor species. Fig. 9 shows the reaction paths of H₂O-related reactions in the combustion zone.

The analysis of reaction paths revealed that the oxygen atom exchange:



and the hydroperoxy-water reaction:



have the most impact on the fuel consumption in the combustion zone. Fig. 10 depicts a change in the production rates of OH and H₂O by oxygen atom exchange (Eq. 24) and hydroperoxy-water reactions (Eq. 25) in comparison to the total production rates.

Injecting additional steam into the combustion zone intensifies H₂O dissociation into hydroxy radicals and hydrogen peroxide. This leads to a displacement of fuel species from reactions with oxygen and its radicals. Fig. 10 shows that both hydroxy and H₂O production rates in the system are reduced when high amounts of steam are injected.

In terms of combustion products, injecting steam has only a minor effect. However, it plays a greater role in temperature regulation. As shown in Fig. 11, the injection of steam can result in a difference of up to 500 K in the temperature of the combustion zone. Thus, more steam is injected into the combustion zone, the lower the combustion temperature is.

Based on the results, shown in Figs. 7 and 11 and Table 3, it is possible to build a correlation between steam injection and consumed fuel for the isochoric combustion zone:

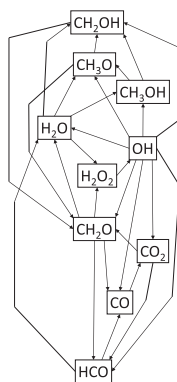
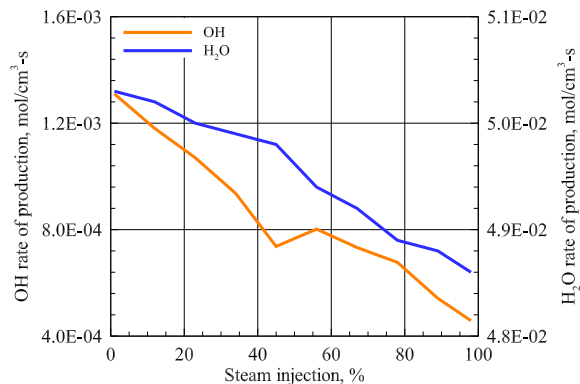
$$F_{24} = \frac{A - F_{34}}{B} \quad (26)$$

Variables A and B are functions of λ :

$$A = 42.55\lambda - 1.9362 \quad (27)$$

$$B = 10.96\lambda + 16.5589 \quad (28)$$

Eqs. (26)–(28) make it possible to pre-calculate the fuel slip based on the designated λ value, and consequently reduce the number of variables at the second stage of optimization. This correlation

**Fig. 9.** Reaction path diagram for H₂O and OH.**Fig. 10.** The effect of steam injection on the total OH and H₂O rates of production in the combustion zone.

can also be used as a method for estimating the expected fuel slip and evaluating the recirculation zone volume and the reactor residence time. For cases 5 – 8 the Eq. 26 is used to calculate the fuel slip and additional steam amount.

2.8. Model optimization – second stage

Next, the remaining mass stream fractions need to be defined. For this purpose, the second optimization stage based on the Multi-Objective Genetic Algorithm (MOGA) (Gupta and Gupta, 2019) was implemented in the commercial code modeFrontier® (ESTECO, 2017). The mean square root error in the case of ROM and CFD for the main species and temperature at the outlet was used as an optimization criteria. The coupling mass stream fractions shown in Fig. 5 were varied in order to minimize the mean square root error for the ROM and CFD for each main species and temperature at the outlet. Table 4 shows the variables and the range, within which the optimization was carried out.

The second stage of optimization was applied only to Case 1 (Voloshchuk et al., 2017). In total, 11000 single calculations were performed. Since the reactor and burner geometries are the same and only the boundary conditions are modified, the flow field and fluid dynamics barely change across all the cases. Therefore, the optimal stream fractions defined for Case 1 were applied to Cases 2–8.

The ROM outlet conditions taken from the outlet zone ($r = 8$) shown in Fig. 5 were used for comparison with the CFD outlet conditions. The square root error was minimized by adjusting mass stream fractions within the ranges shown in Table 4.

The MOGA algorithm was also used for the sensitivity analysis of the model. It can be concluded that the most sensitive zone in the ROM is the combustion zone. The definition of this zone dictates the definition of other zones and values of the stream functions. The model sensitivity in the regard to the combustion zone was demonstrated in Section 2.5. Additionally, Fig. 6 demonstrates model sensitivity to the number of segments used for modeling plug-flow zone. It was shown that an increase in the plug-flow resolution increases the model accuracy to a certain extent.

3. Results

3.1. ROM Results

Table 5 lists the volumes of each zone in the reactor calculated by the ROM for all cases. As indicated, the reactor geometry significantly varies from 40 to 455 l which allows for model validation against results obtained from reactors of different geometries.

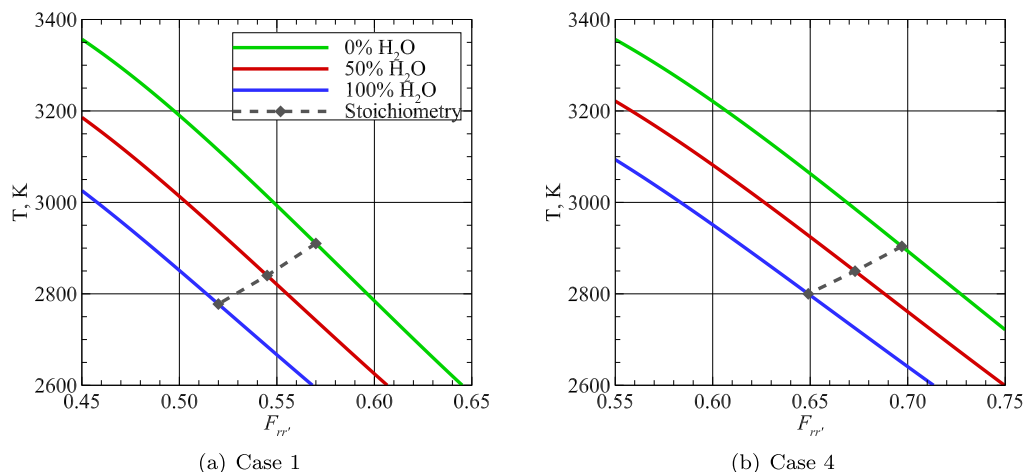


Fig. 11. Sensitivity of the combustion zone to fuel and moderator injections. Blue, red, and green graphs show influence of fuel injection on the combustion temperature when 100%, 50%, and 0% of moderator is injected in the combustion zone, respectively. Gray line shows the position at which stoichiometric criterion is satisfied.

Table 4
Optimization variables for Case 1.

Variable	Range	Step
F_{24}	0.52	0.01
F_{25}	$0.01 \div 0.48$	
F_{27}	$1 - F_{24} - F_{25}$	
F_{34}	0.98	
F_{35}	0.01	0.01
F_{37}	0.01	
F_{45}	$0.01 \div 0.99$	
F_{47}	$1 - F_{45}$	
F_{67}	$0.01 \div 0.99$	0.01
F_{68}	$1 - F_{67}$	

The volume of the combustion zone ($r = 4$) is shown in ml since it is the smallest volume in the domain. Unlike other zones volumes, the volume of the combustion zone fluctuates between the cases since it is derived from the inlet properties of the reactants, e.g., oxidizer, fuel, and moderator velocities, and nozzle geometry (see Eq. 1 and 2).

Table 6 lists the results at the reactor outlet for all simulated cases. Additionally, the absolute error in temperature between ROM and experiments is shown. To indicate the deviation in composition between ROM and experiments, a Root-Mean-Square (RMS) of relative error in composition was calculated.

The most indicative case among all calculations is case 1. The ROM was optimized specifically for this case and the results of optimization were applied to all other cases. As shown, the deviation between experiments and ROM for cases 2, 3, 5–8 is even lower than in case 1. This means that the ROM can accurately predict outlet composition for the reactors even with different reactor and burner geometries. Case 4, however, stands out in this regard. The observed high RMS deviation between ROM and experiments is due to an extremely low CH_4 concentration at the outlet. The calculated value is 0.02 mol% while the measured value is 0.06 mol%.

Table 5
Volume of each zone calculated by ROM for each test case.

Zones index r	Units	Case 1	Case 2	Case 3	Case 4	Case 5	Case 6	Case 7	Case 8
$r = 4$	ml	44	45	44	50	38	30	28	35
$r = 5 + r = 6$	l	234	234	234	234	17	57	57	57
$r = 7$	l	221	221	221	221	24	65	65	65
$r = 8$	l	0.3	0.3	0.3	0.3	0.5	2	2	2
Total	l	455	455	455	455	41	120	120	120

Thus, the relative error is 67%, resulting in an overall high RMS deviation. The results are also in good agreement in terms of outlet temperature. It is possible to conclude that the developed ROM can provide accurate results for the HP-POX systems, while utilizing minimum computational power.

The computation time for a single steady-state ROM calculation is less than 1 min on a single computational core. A reference CFD calculation in 2D requires approximately 4 days on a high-performance cluster computing node with 20 cores.

3.2. Comparison between ROM, CFD, and experimental results

Fig. 12 shows the results of the ROM simulations, experiments, and CFD calculations at the outlet for Cases 1 and 4. The second stage of optimization was used only for Case 1, while the first stage of optimization was carried out for all cases.

The results of the ROM are in good agreement with both the CFD and experiments. The fact that the stream fractions $F_{rr'}$ do not change from case to case, yet sustain the accuracy of the results indicates that the flow field characteristics depend on the reactor geometry but not on boundary conditions in the simulated cases.

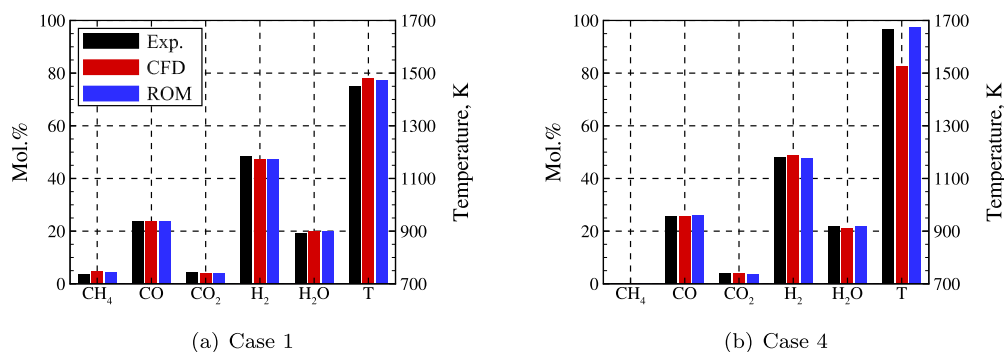
The average absolute error in the results of the ROM and CFD for all calculations in the methane concentration at the outlet is 0.30%. The average difference in temperature for all calculations is 26.42 K. Additionally, Fig. 12 provides a comparison between the ROM and experiments. The average absolute error in the results of the ROM and experiments in methane concentration at the outlet is 0.19% and the highest absolute error is observed for H_2 with 0.70%. The average temperature difference is 15.95 K. Table 7 lists the absolute errors in the ROM, CFD and experimental results.

As shown, the ROM is capable of producing accurate results in terms of global reactor characteristics. The first stage of optimization is essential for a robust solution, since the combustion zone is the most important aspect and defines the fuel slip in the system. The ROM global reactor characteristics mainly depend on the fuel

Table 6

Results of the ROM calculations and comparison to the experiments.

	Units	Case 1	Case 2	Case 3	Case 4	Case 5	Case 6	Case 7	Case 8
CH ₄	mol%	4.39	4.52	5.03	0.02	0.37	0.10	0.36	0.30
CO	mol%	23.68	23.64	23.60	25.86	27.45	24.58	26.15	26.68
CO ₂	mol%	4.03	3.95	3.91	3.60	3.09	3.77	5.07	3.18
H ₂	mol%	47.38	47.49	47.32	47.79	49.35	46.66	42.79	49.39
H ₂ O	mol%	19.99	19.68	19.50	22.02	18.69	24.62	24.98	20.08
T	K	1473	1474	1476	1675	1689	1707	1651	1699
T _{Error}	K	22.49	25.34	30.92	9.03	−1.31	10.78	13.04	14.65
RMS		7.88	4.43	5.76	30.01	6.39	5.49	2.77	4.88

**Fig. 12.** Comparison of the ROM, CFD, and experimental results.

slip calculations. The second stage of optimization permits error reduction and accuracy adjustments within a narrow range.

The basic flow field pattern can be characterized by the impulse response function, which shows how the system reacts to an impulse introduced at the inlet. Transient ROM and CFD calculations with an identical setup are carried out to compare the resulting impulse response function. The calculation time was set to 1000 s, with a time step of 0.1 s. The tracer is injected at the inlet in the first time step, resulting in a short impulse of 1 ms. The tracer is measured at the reactor outlet and integrated. Fig. 13 compares the accumulated tracer signals at the outlet, based on ROM and CFD calculations for Cases 1 and 4. As shown, the tracer amount sums to one, which indicates the accuracy of the numerical schemes. The steepness of the curve is affected by the reactor volume. Reactors with a smaller volume and a smaller residence time exhibit a steeper curve. From preliminary studies it can be concluded that the mass stream functions affect the impulse response. Also, the fuel slip plays a significant role, whereas the influence of the second stage of optimization is minor.

In this work, the second stage of optimization was applied only to Case 1 and the mass stream fractions calculated for Case 1 were used for all other cases, but the comparison of the ROM data against CFD and experimental results shows a high accuracy of the model. This indicates that the model optimized for Case 1 can be used for analysis and calculations of other reactor and burner geometries of similar type without the need for additional optimization.

Table 7

Absolute errors in outlet composition and temperature between ROM, CFD, and experimental results.

	Units	ROM-CFD	ROM-Exp.
CH ₄	mol%	0.30	0.19
CO	mol%	0.35	0.17
CO ₂	mol%	0.15	0.30
H ₂	mol%	0.36	0.70
H ₂ O	mol%	0.37	0.61
T	K	26.42	15.95

Fig. 13 illustrates the very good agreement between ROM and CFD impulse response calculations, meaning that the ROM can reproduce basic reactor physics and flow field pattern by using a PSR network. The steepness of the impulse response curve mainly depends on F_{67} coupled with F_{68} and F_{47} , coupled with F_{45} mass stream fractions. However, the global reactor characteristics are only slightly influenced by adjustments to the impulse response function. A fluctuation of less than 1% from the optimal values for the outlet composition and temperature was observed during the variation of the F_{67} , F_{68} , F_{47} , and F_{45} mass stream fractions. A greater effect in terms of the residence time distribution is observed when the reactor zone volumes are changed.

The impulse was fully transported through the reactor in Cases 1–4 within the first 70 s. As shown, the first response was received within 4 s of the simulation. The smaller reactor volume in other cases reduces the impulse response time proportionally to the volume. The designed gas residence time is calculated as:

$$\tau = \frac{\dot{V}}{\bar{V}}, \quad (29)$$

where \dot{V} is the volumetric flow rate and τ is the gas residence time, corresponds to a response time when 60% of the impulse was measured. This means that 40% of the remaining gas recirculates and needs more time to leave the reactor.

3.3. Influence of local processes on the global reactor characteristics

The ROM provides insights into how the species conversion progresses in the reactive system. Local conversion identifies how much of species volume is converted within a certain reactor zone in comparison to its global conversion. This provides an estimate of the importance of a single zone in terms of global reactor characteristics, and can be used to optimize the reactor geometry, boundary conditions and operating regime. Table 8 shows the species volumetric conversion fractions for different reactor zones as indicated in Fig. 5.

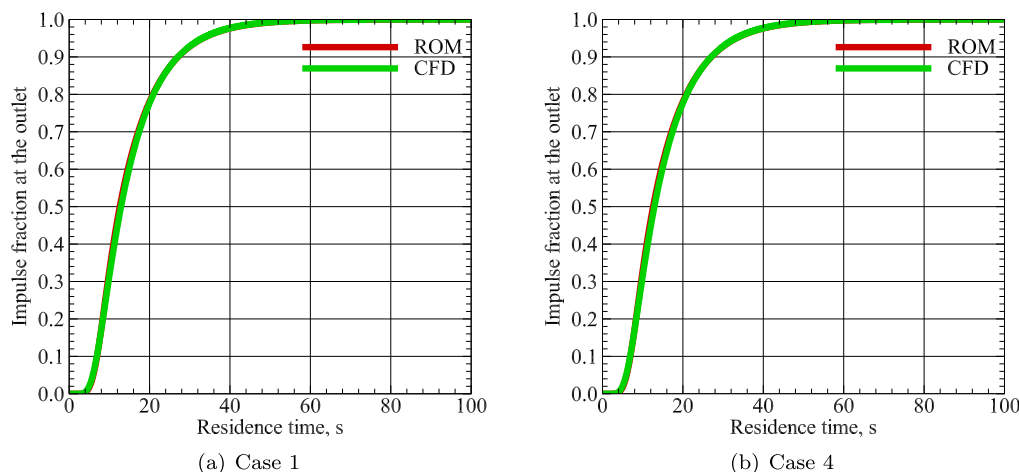


Fig. 13. Integral impulse response at the outlet.

The volumetric conversion fraction is calculated as:

$$\chi_k^r = \frac{\dot{V}_k^{\text{out},r} - \dot{V}_k^{\text{in},r}}{|\dot{V}_k^{\text{out}} - \dot{V}_k^{\text{in}}|}; \sum_r \chi_k^r = \pm 1, \quad (30)$$

where χ is the conversion fraction of the k th species in reactor zone r , \dot{V} is the volumetric flow rate in Nm^3/hr , and the superscripts "in" and "out" denote the inlet and outlet of the reactor zone, respectively. Summing the single species conversion fractions over all the reactor zones results in 1, but can be either positive or negative. Here, a negative sign before a fraction value indicates the consumption of the species in a given reactor zone, while a positive sign indicates production.

It should be noted that values higher than 1 indicate that local species production/consumption is much higher than the conversion of this species in the reactor, calculated as the difference in volumetric flow rates between the global reactor outlet and inlet. According to the results listed in Table 8, more than 57% of overall methane conversion occurs in the combustion zone. However, over 30% of conversion also takes place in the recirculation zone and less than 10% occurs in the bypass and plug-flow zones. Most of the carbon monoxide is produced in the combustion zone, where over 60% of overall CO conversion occurs. In addition, a large amount of CO_2 and H_2O is released from the combustion zone due to redox reactions.

Most of the H_2O is later consumed in the recirculation zone, but a significant part is also consumed in the bypass and plug-flow zones. The recirculation zone plays also an important role in hydrogen formation since over 40% of total hydrogen production occurs there. Compared to Case 1, Case 4 has a higher λ value and, therefore a higher fuel consumption in the combustion zone. Table 9 shows the local conversion of species in different reactor zones for Case 4.

As indicated in Table 9, the combustion zone plays the most important role in fuel consumption and the production of syngas. Despite the smaller fuel slip, the fraction of methane consumption

in the recirculation zone is barely changed for all the cases. The same tendency is observed in relation to H_2 production. The hydrogen production fraction in the combustion zone is increased by almost 10% from Case 1 to Case 4, but remains almost constant in the recirculation zone.

It can be concluded that conversion in the combustion zone depends on fuel/oxygen mixing, regulated by the boundary conditions and burner geometry. The combustion zone has the biggest influence on the process, but reforming in the recirculation and plug-flow zones is not negligible and can be influenced by the reactor geometry modifications.

The increase in the plug-flow zone volume results in an increase in CH_4 conversion into syngas. This effect is indicated in Table 10. The plug-flow zone was increased by 10 times from its original size, while the rest of the reactor remained unchanged. In reality this would mean the prolongation of the plug-flow zone without changing the diameter of the reactor. In this case, the recirculation and the combustion zones would not be influenced in terms of gas processing. As shown in Table 10, the consumption of CH_4 and production of CO and H_2 would increase. The conversion fraction of H_2O is lower in the bigger plug-flow zone due to the increase in overall H_2O consumption.

Fig. 14 shows a comparison of the results obtained with the ROM for the original reactor configuration and the reactor with a prolonged plug-flow zone. The equilibrium results are also given. The increase in the reactor volume shortens the distance to equilibrium. However, the results do not justify the prolongation of the plug-flow zone 10 times from the economic point of view. Even in the larger reactors, the combustion zone shows dominance over the other reactor zones. For the cases, such as Case 4–8, with close-to-equilibrium outlet conditions like Case 4, the increase in the reactor volume plays a minor role, meaning that local conversion fractions are not greatly influenced by a further increase in the reactor volume. For the cases which are far from equilibrium, such as Case 1, 2, and 3, where the CH_4 concentration at the outlet is very high, adjustments to the inlet boundary conditions or burner

Table 8
Species conversion in each reactor zone for Case 1, $\frac{\text{Nm}^3/\text{hr}}{\text{Nm}^3/\text{hr}}$.

Zone ID	CH_4	CO	CO_2	H_2	H_2O
4	−0.57	+0.65	+1.18	+0.37	+48.54
5 and 6	−0.09	+0.09	−0.07	+0.18	−16.97
7	−0.33	+0.26	−0.11	+0.45	−32.58
8	0	$+1 \cdot 10^{-4}$	$+8 \cdot 10^{-4}$	0	0

Table 9Species conversion in each reactor zone for Case 4, $\frac{\text{Nm}^3/\text{hr}}{\text{Nm}^3/\text{hr}}$.

Zone ID	CH ₄	CO	CO ₂	H ₂	H ₂ O
4	−0.66	+0.72	+1.31	+0.46	+5.95
5 and 6	−0.04	+0.04	−0.05	+0.08	−0.89
7	−0.30	+0.24	−0.26	+0.46	−4.06
8	0	0	0	0	0

Table 10Species conversion in plug-flow zones of different volumes for Case 1, $\frac{\text{Nm}^3/\text{hr}}{\text{Nm}^3/\text{hr}}$.

Plug-flow zone volume	CH ₄	CO	CO ₂	H ₂	H ₂ O
$10 \times V_{\text{PFZ}}$	−0.12	+0.11	−0.07	+0.22	−3.59
V_{PFZ}	−0.09	+0.09	−0.07	+0.18	−16.97

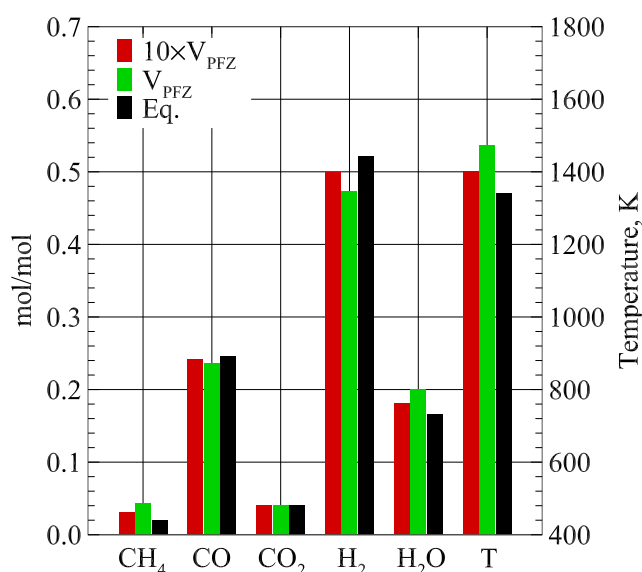


Fig. 14. Comparison of outlet composition and temperature for the reactors with different plug-flow zone volumes. Green color indicates values for case 1, red color indicates values for the same reactor but with increased plug-flow zone volume, black color shows equilibrium thermo-chemical state.

geometry might bring higher benefit to the system than adjustments to the reactor geometry.

4. Conclusion

In the present work, a ROM was developed for natural gas POX processes. The ROM can reproduce not only global reactor characteristics but also basic flow field patterns in terms of the similitude of the impulse response function. This allows the model to be coupled with optimization algorithms, which can be used for process optimization, e.g., adjusting boundary conditions and burner or reactor geometries. The ROM was validated against previously conducted CFD investigations on the Virtuhcon Benchmark and recent large-scale experiments, which comprises eight test cases with different operating pressures and outlet temperatures. It was shown that the model is robust and can be used for different reactor and burner configurations as well as for various boundary conditions without the need for additional model optimization.

Based on the ROM results, the following conclusions can be made:

1. The ROM is capable of correctly reproducing both CFD and experimental results in terms of the outlet composition.

2. The ROM can reproduce basic flow field patterns taken from CFD calculations, e.g., the impulse response function.
3. The most significant process in the POX system is the oxidation of fuel. Most of the syngas production occurs in the combustion zone.
4. The reforming section of the reactor becomes more important at a bigger distance from equilibrium. The overall conversion can be improved by adjusting the reactor volume.

Apart from global process analysis, the ROM helped to investigate how the conversion processes depended on the steam injection. As a result, a unified correlation was proposed to estimate the fuel slip from the burner to the downstream reactor sections. The more steam injected along with oxidizer and fuel, the lower the combustion temperature, the bigger the fuel slip, and the more intense the formation of H and OH radicals via H₂O-related reactions.

CRediT authorship contribution statement

Yury Voloshchuk: Methodology, Software, Validation, Writing – original draft. **Andreas Richter:** Conceptualization, Writing – review & editing.

Declaration of Competing Interest

The authors declare that they have no known competing financial interests or personal relationships that could have appeared to influence the work reported in this paper.

Acknowledgments

We would like to thank the Federal Ministry of Education and Research of Germany for supporting this work in the framework of OptiCon (funding number 03Z22F513).

References

- Aasberg-Petersen, K., Hansen, J.H.B., Christensen, T.S., Dybkjaer, I., Christensen, P.S., Nielsen, C.S., Madsen, S.E.L.W., Rostrup-Nielsen, J.R., 2001. Technologies for large-scale gas conversion. *Appl. Catal. A: General* 221, 379–387.
- Aminand, N.A.S., Yaw, T.C., 2007. Thermodynamic equilibrium analysis of combined carbon dioxide reforming with partial oxidation of methane to syngas. *Int. J. Hydrogen Energy* 32, 1789–1798.
- ANSYS Chemkin-Prot V 17.2 (2016).
- Brüggemann, P., Seifert, P., Meyer, B., Müller-Hagedorn, M., 2010. Influence of temperature and pressure on the non-catalytic partial oxidation of natural gas. *Chem. Prod. Proc. Model.* 5, 1–27.
- Bustamante, F., Enick, R., Cugini, A., Killmeyer, R., Howard, B., Rothenberger, K., Ciocco, M., Morreale, B., Chattopadhyay, S., Shi, S., 2004. High-temperature kinetics of the homogeneous reverse water-gas shift reaction. *AIChE J.* 50, 1028–1041.

- Cerbe, G., Lendt, B., 2016. Grundlagen der Gastechnik: Gasbeschaffung – Gasverteilung – Gasverwendung. Carl Hanser Verlag GmbH & Company KG. ESTECO modeFrontier, 2017. URL www.ESTECO.com.
- Fornaciari, N., Schefer, R., Paul, P., Sanford, R., Clayton, L., Lubeck, C., 1994. User guide to the burner engineering research laboratory. Sandia National Laboratories.
- Förster, T., Voloshchuk, Y., Richter, A., Meyer, B., 2017. 3d numerical study of the performance of different burner concepts for the high-pressure non-catalytic natural gas reforming based on the freiberg semi-industrial test facility hp pox. Fuel 203, 954–963.
- Goodwin, D.G., Speth, R.L., Moffat, H.K., Weber, B.W., 2018. Cantera: An Object-oriented Software Toolkit for Chemical Kinetics. Thermodyn. Transport Processes. URL <https://www.cantera.org>.
- Guiberti, T.F., Krishna, Y., Boyette, W.R., Yang, C., Roberts, W.L., Magnotti, G., 2020. Single-shot imaging of major species and oh mole fractions and temperature in non-premixed H₂/N₂ flames at elevated pressure. Proc. Combust. Inst. 000, 1–9.
- Gupta, K., Gupta, M.K., 2019. Optimization of Manufacturing Processes. Springer.
- Han, S., Park, J., Song, S., Chun, K.M., 2010. Experimental and numerical study of detailed reaction mechanism optimization for syngas (H₂+CO) production by non-catalytic partial oxidation of methane in a flow reactor. Int. J. Hydrog. Energy 35, 8762–8771.
- Higman, C., van der Burgt, M., 2003. Gasification. Gulf Professional Publishing.
- Li, C., Burke, N., Gerdes, K., Patel, J., 2013. The undiluted, non-catalytic partial oxidation of methane in a flow tube reactor – an experimental study using indirect induction heating. Fuel 109, 409–416.
- Li, C., Kuan, B., Lee, W.J., Burke, N., Patel, J., 2018. The non-catalytic partial oxidation of methane in a flow tube reactor using indirect induction heating – an experimental and kinetic modelling study. Chem. Eng. Sci. 187, 189–199.
- Monaghan, R.F.D., Ghoniem, A.F., 2012. A dynamic reduced order model for simulating entrained flow gasifiers. part i: model development and description. Fuel 91, 61–80.
- Monaghan, R.F.D., Ghoniem, A.F., 2012. A dynamic reduced order model for simulating entrained flow gasifiers. part ii: model validation and sensitivity analysis. Fuel 94, 280–297.
- Nezhad, M.Z., Rowshanzamir, S., Eikani, M., 2009. Autothermal reforming of methane to syngas: modeling and simulation. Int. J. Hydrogen Energy 34, 1292–1300.
- Olivieri, A., Veglio, F., 2008. Process simulation of natural gas steam reforming: fuel distribution optimization in the furnace. Fuel Proc. Technol. 89, 622–632.
- Pedersen, L.S., Breithaupt, P., Dam-Johansen, K., Weber, R., 1997. Residence time distributions in confined swirling flames. Combust. Sci. and Tech. 127, 251–273.
- Pedersen, L.S., Glarborg, P., Dam-Johansen, K., Hepburn, P.W., Hesselmann, G., 1998. A chemical engineering model for predicting no emissions and burnout from pulverized coal flames. Combust. Sci. and Tech. 132, 251–314.
- Peña, M.A., Gomes, J.P., Fierro, J.L.G., 1996. New catalytic routes for syngas and hydrogen production. Appl. Catal. A: General 144, 7–57.
- Rehm, M., Seifert, P., Meyer, B., 2009. Theoretical and numerical investigation on the edc-model for turbulence-chemistry interaction at gasification condition. Comput. Chem. Eng. 33, 402–407.
- Richter, A., Seifert, P., Compart, F., Tischer, P., Meyer, B., 2015. A large-scale benchmark for the cfd modeling of non-catalytic reforming of natural gas based on the freiberg test plant hp pox. Fuel 152, 110–121.
- Siang, T.J., Jalil, A.A., Abdulrasheed, A.A., Hambali, H.U., Nabgan, W., 2020. Thermodynamic equilibrium study of altering methane partial oxidation for fisher-tropsch syngas production. Energy 198, 117394.
- Silva, O., 2003. Numerical simulation of the reactive flow in a combustion chamber PhD dissertation. Universidade de Évora, Évora.
- Smith, G., Golden, D., Frenklach, M., Moriarty, N., Eiteneer, B., Goldenberg, M., Bowman, C., Hanson, R., Song, S., Gardiner, Jr., W., Lissianski, V., Qin, Z., 1999. GRI-Mech 3.0. URL www.me.berkeley.edu/gri_mech/.
- Somarathne, K.D.K.A., Okafor, E.C., Sugawara, D., Hayakawa, A., Kobayashi, H., 2020. Effects of oh concentration and temperature on no emission characteristics of turbulent non-premixed CH₄/NH₃/air flames in a two-stage gas turbine like combustor at high pressure. Proc. Combust. Inst. 000, 1–8.
- Toni, A.D., Hayashi, T., Schneider, P., 2013. A reactor network model for predicting nox emissions in an industrial natural gas burner. J. Braz. Soc. Mech. Sci. Eng. 35, 199–206.
- Ullman's Encyclopedia of Industrial Chemistry, 2003.
- van der Burgt, M., van Keeuwen, C.J., del'Amico, S.T.S.J.J., 1988. The shell middle distillate process (smds). Stud. Surf. Sci. Catal. 36, 473–482.
- van Helvoort, T., Senden, V.M., 2014. Gas to liquids: historical development of GTL technology in Shell. Shell international B.V.
- Vascellari, M., Xu, H., Hartl, S., Hunger, F., Hasse, C., 2015. Flamelet/progress variable modeling of partial oxidation systems: from laboratory flames to pilot-scale reactors. Chem. Eng. Sci. 134, 694–707.
- Velasco, J.A., Lopez, L., Cabrera, S., Boutonnet, M., Järas, S., 2014. Synthesis gas production for gtl applications: thermodynamic equilibrium approach and potential for carbon formation in a catalytic partial oxidation pre-reformer. J. Natural Gas Sci. Eng. 20, 175–183.
- Voloshchuk, Y., Vascellari, M., Hasse, C., Meyer, B., Richter, A., 2017. Numerical study of natural gas reforming by non-catalytic partial oxidation based on the virtuhcon benchmark. Chem. Eng. J. 327, 307–319.
- Xu, Y., Dai, Z., Li, C., Li, X., Zhoy, Z., Yu, G., 2014. Numerical simulation of natural gas non-catalytic partial oxidation reformer, International Journal of Hydrogen. Energy 39, 9149–9157.
- Yang, X., Peng, Z., Ding, Y., Du, Y., 2021. Temperature and oh concentration measurements by ultraviolet broadband absorption of oh(x) in laminar methane/air premixed flames. Fuel 288, 119666.
- Yu, Z., Cao, E., Wang, Y., Zhou, Z., Dai, Z., 2006. Simulation of natural gas steam reforming furnace. Fuel Proc. Technol. 87, 695–704.
- Zamaniyan, A., Ebrahimi, H., Mohammadzadeh, J.S., 2008. A unified model for top fired methane steam reformers using three-dimensional zonal analysis. Chem. Eng. Proc. 47, 946–956.
- Zhai, X., Ding, S., Cheng, Y., Jin, Y., Cheng, Y., 2010. CFD simulation with detailed chemistry of steam reforming of methane for hydrogen production in an integrated micro-reactor. Int. J. Hydrog. Energy 35, 5383–5392.